Imaging of THz photonic modes by scattering scanning near-field optical microscopy

L. Thomas, Theo Hannotte, Cristiane N. Santos, Benjamin Walter, Melanie Lavancier, Sophie Eliet, Marc Faucher, Jean-Francois Lampin, Romain Peretti

IMAGING OF THZ PHOTONIC MODES BY SCATTERING SCANNING NEAR-FIELD OPTICAL MICROSCOPY *

L. Thomas †, T. Hannotte †, C. N. Santos †, M. Lavancier, S. Eliet, M. Faucher, J.-F. Lampin, R. Peretti
Institut d'Electronique, de Microélectronique et de Nanotechnologie,
CNRS, Univ. Lille,
Villeneuve d'Ascq, 59652 France

B. Walter
Vmicro SAS
Villeneuve d'Ascq, 59650 France

Corresponding author
romain.peretti@iemn.univ-lille1.fr
† Authors contributed equally to this work

ABSTRACT

We investigated the near-field distribution associated to the photonic mode of terahertz photonic micro-resonators by scattering scanning near-field optical microscopy. Probing individual THz micro-resonators concentrating electric field is important for high-sensitivity chemical and biochemical sensing and fundamental light-matter interactions studies at nanoscale. We imaged both electric field concentration predicted by numerical simulations and unexpected patterns that deviate from intuitive assumptions. We propose a scenario based on the multiplication of the near-field with the far-field pattern of the probe / resonator ensemble that is in excellent agreement with the experimental data and propose an image analysis procedure to recover the near-field of such structures.

***K*eywords** Photonics · terahertz · resonators · microscopy · s-SNOM

1 Introduction

Sensing with terahertz (THz) radiations (100 GHz – 10 THz, λ : 3 mm – 30 µm) has demonstrated valuable purposes, *e.g.* for the uncovering of hidden items or the detection of relevant chemical and bio-chemical compounds [1, 2, 3]. However, given that rather long wavelengths are used, addressing single objects smaller than a few hundredths of mm is not accessible to traditional diffraction-limited optical systems that detect far-field (FF) radiation [4]. Achieving sub-λ (typically $< 100\,\mu\mathrm{m}$) THz sensing requires the integration of photonic resonators confining light into narrow volumes, in the non-propagating near-field (NF), to probe minutes amounts of material [5, 6]. Confinement of THz electric field is not only of interest for applied purposes, *e.g.* characterization of a single micro-object in a resonator [7] or building 2D materials-based THz modulators [8], but also for fundamental investigations on THz sub-λ ultrastrong light-matter interactions [9]. Such THz micro-resonators are typically used as meta-atom tailoring the dispersion properties of metasurfaces when assembled in arrays [10]. For the aforementioned examples, knowledge of both the resonators and the assemblies is a key step in these studies. Whereas large arrays of THz photonic micro-resonators can be routinely studied by THz time-domain spectroscopy (THz-TDS) in the FF [11, 12], characterization of individual micro-resonators requires to probe beyond the diffraction limit. In this framework, several THz microscopy techniques have been developed, relying on the detection of the evanescent NF. Typically, these schemes detect the interactions

* *Citation*: **L. Thomas, T. Hannotte, C. N. Santos *et al.*. Imaging of THz Photonic Modes by Scattering Scanning Near-field Optical Microscopy. Pages.... DOI:000000/11111.**

between THz radiation, the sample and a raster-scanning sub-λ probe [13]. Different imaging apparatus and NF probes have been explored to reach sub-λ resolution: In THz emission microscopy, the probe is a focused femtosecond laser beam of shorter wavelength interacting with the sample, or the substrate beneath, to emit THz radiation [14]. Otherwise, solid probes illuminated by THz radiation such as photoconductive (PC) detectors [15, 16, 17], electro-optic (EO) sensors [18], waveguides [19] or tips with [20] or without aperture [21] have demonstrated the ability to detect the NF. It is also worth to mention that out of scanning microscopy schemes, real-time THz microscopy has been demonstrated, but requires objects to be placed on EO crystals [22]. To date, the highest resolution, ($< 15\,\mathrm{nm}$) was achieved through an apertureless technique known as scattering scanning near-field optical microscopy (s-SNOM) [23]. s-SNOM imaging uses the cantilevered tip of an atomic force microscope (AFM) to concentrate and elastically scatter light from the NF to the FF detection while recording simultaneously the AFM topography [24, 25, 26]. Since its transposition to the THz domain, s-SNOM has been recognized as a promising tool for the study of relevant materials and devices for electronics and optoelectronics [27, 28, 29, 30, 31, 32, 33, 34, 35], and even biomaterials [36], micro-organisms [37] or proteins [38]. In addition, THz s-SNOM has also demonstrated the ability to image sub-surface patterns [39] and to probe shape-dependent (rather than material-dependent) contrast [40, 41, 42]. Despite vivid interest in the applications of THz s-SNOM, so far, to the best of our knowledge, only one study focused on photonic resonators [43]. On the contrary, in the infrared (IR) domain, successful s-SNOM imaging of these systems have been already reported through the literature [44, 45, 46, 47, 48, 49, 50, 51]. When applied to photonic resonators, in addition to material-related contrast, s-SNOM imaging reveals the localized electric fields scattered by the tip at sub-λ scale and is therefore a promising technique to probe single micro-resonators with high spatial resolution. Disregarding the challenge of traditional bulky THz sources and detectors, the current state-of-the-art is rather intriguing since THz resonators are larger, and thus relatively easier to manufacture than their IR counterparts. In this paper, we investigate two typical THz micro-resonators: large bandwidth two-arm logarithmic spiral antennas (LSAs) and narrow bandwidth split-ring resonators (SRRs). SRRs concentrate electric field in their gap when receiving electromagnetic waves matching their inductor-capacitor resonance. Various designs of THz SRRs and complementary SRRs have been studied at larger scale with other imaging techniques, *i.e.*, with PC and EO detectors [52, 53, 54, 55], emission microscopy [56], tapered dipole antenna sensor [57], apertureless microscopy [58] and real-time THz microscopy [59]. Meanwhile, to the best of our knowledge, THz spiral antennas were not imaged in the NF so far. In the course of our study, we address the following points:

1. After designing resonators through finite difference time domain (FDTD) simulations and probing their transmission properties by THz-TDS, we performed NF characterization. We found that THz s-SNOM imaging is able to resolve spatial features associated with the photonic mode of the resonators. Surprisingly, we also recorded other features that strongly deviate from assumptions based on computed NF distributions.
2. Since these particular features were not previously reported for their IR counterparts, or other works in the THz domain, we discuss on the mechanisms responsible for detecting s-SNOM signal when a photonic micro-resonator is under the tip. On the basis of more sophisticated simulations, we propose a scenario to account for the discrepancy.
3. The excellent agreement between the proposed scenario and the experimental data led us to identify an experimental bottleneck originating from spatial multiplication of NF and FF. We emphasize that this unexpected effect must be carefully handled in future works.
4. Finally, we propose an image analysis algorithm to circumvent the issue. Albeit not applicable to every photonic resonators, it allows to recover the NF mapping of a SRR.

2 Results

We first designed LSAs and SRRs to match the 2.5 THz emission frequency of a CO_2 pumped methanol gas laser. Through FDTD simulation, we computed on HR-Si substrates the transmission spectra of gold LSAs and SRRs. The selected designs are the following: for the LSAs, 110 µm diameter antennas with non-terminated arms and a bowtie center, and for the SRRs a square double geometry. Computed transmission spectra exhibit the expected features: for the LSAs, an absorption over the 0.5 – 3.5 THz range (Figure S1, a), while the spectra of the SRRs showed a narrow absorption band whose center was determined by the length (l) and gap size (g) of the resonators. For the next steps of our study, we selected SRRs tuned to 2.5 THz ($l = 13\,\mu\mathrm{m}, g = 2\,\mu\mathrm{m}$) (Figure S1, b) and detuned SRRs ($l = 17\,\mu\mathrm{m}, g = 2\,\mu\mathrm{m}$) for the purpose of control experiments (Figure S1, c).

We also computed the NF spatial distribution of the LSA and the tuned SRR when receiving 2.5 THz incident radiation. The LSA NF distribution exhibited alternating dark and bright regions on the arms with a concentration of the field at the center of the antenna (Figure 2, a, c). Superior confinement is predicted for the SRR: the electric field of the photonic mode is located in the gap and extend slightly over the arms of the capacitor (Figure 3, a, d). NF distributions

were computed in a plane parallel to the substrate 250 nm above the resonators and we only considered the vertical component (E_z) of the NF that couple efficiently with the geometry of the s-SNOM tip [60].

The micro-resonators were fabricated following standard electron beam lithography process (see methods) and subsequently probed by THz-TDS under nitrogen atmosphere. Note that due to the sensitivity of THz-TDS the measurements of a single resonator is not possible. Consequently, we measured arrays of micro-resonators. For both the LSA (Figure S1, a), the tuned SRR (Figure S1, b) and the detuned SRR (Figure S1, c), transmission spectra were in good accordance with the FDTD simulations and did not exhibited any other spectral feature.

Following these observations by THz-TDS, we investigated the NF properties of the micro-resonators by s-SNOM.

We employed a standard s-SNOM apparatus where the incident beam (2.5 THz, continuous wave, vertically polarized) pass through a Michelson interferometer and is focused on the tip with a truncated parabolic mirror (Figure 1, a, b). In the following, we label the direction from the head of the microscope to the mirror as the North-South (N-S) axis, as indicated on (Figure 1, a, b). This mirror is placed in front of the probe and is also used to collect the scattered NF (electric field component labeled E_s) to which is added a background signal (electric field component labeled E_{bg}). E_{bg} originates from adventitious reflections of the incident beam on the probe and the sample due to the inherent large size of the spot limited by the diffraction. The collected signals are mixed with the reference arm of the interferometer (E_R) before detection (Figure 1, a, b). This configuration is called homodyne detection (HD). The microscope operates in intermittent contact (tapping) mode with the oscillating probe driven close to its eigenfrequency (Ω). Optical signals are demodulated to the higher harmonics of the probe driving frequency ($n\Omega$, n = 1 – 4) to significantly suppress the background signal on s-SNOM images (see methods and Supplementary Information). Except specified otherwise, we show images of the amplitude of the demodulated signal (S_n) recorded for $n = 2$ (S_2). The horizontal and lateral axes of the images correspond respectively to the slow and fast scan axes of the AFM. We quantified the images with the contrast (C) between regions a and b, calculated following eq. 1, where $S_{2\text{a,b}}$ is the average measured signal, demodulated at 2Ω, in regions a and b. In our case, region a is the part of interest of the resonator and b the surrounding substrate. The calculated contrasts are summarized in the Supporting Information (Table S2).

$$C = 100 \times \left(\frac{S_{2\text{a}} - S_{2\text{b}}}{S_{2\text{b}}} \right). \tag{1}$$

We first imaged a LSA (selected in a metasurface). The THz s-SNOM image exhibits bright and dark regions distributed along the arms of the antenna (Figure 2, b) while the simultaneously recorded topography only shows the flat surface of the LSA (Figure 2, d). The same feature is recovered for demodulation at other harmonics of Ω (n = 1 - 4) (Figure S2, a – d). The brightest regions on arms A and B (arms labeled as on Figure 2, b) with higher field confinement show respectively +35 and +49 % maximum contrast with respect to the HR-Si substrate.

This pattern is similar to the computed NF distribution that also shows alternating bright and dark regions (Figure 2, a). It also appears clearly on profiles taken across the arms (Figure 2, c) that the THz s-SNOM image does not exhibit point-symmetry with respect to the center of the spiral and that the maximum of scattered NF is not located on the center of the antenna.

This discrepancy may have several causes that are difficult to identify, *e.g.*, the high amount of reflective metal on this area of the sample may lead to a large background signal that cannot be fully eliminated, or that the tip locally disrupt the symmetry, leading to a complicated interference pattern of traveling waves across the arms.

An additional feature is found at the center of the LSA: the probe of the arm A is darker than the substrate (C: -43 %) while the probe of arm B is brighter (C: +18 %) (Figure 2, b), again, the topography does not show any difference between the two arms (Figure 2, d) and the same effect is observed for all harmonics, indicating that this pattern does not originate from the background (Figure S2, a – d). This unexpected effect is strongly localized at the core of the resonator and was not predicted by computations.

Whereas asymmetry in s-SNOM images was not reported on previous work with LSA in the infrared [50], Büchner *et al.* recorded similar patterns on plasmonic antennas [61]. In this work, authors attribute the asymmetry to the modification of the resonance of the antenna when strong coupling occurs between the tip and the antenna.

Similarly, we hypothesize that the assymetry at the center of the LSA is a signature of the interaction between the probe and the NF on the bowtie probes where high confinement was expected. To gain more insight into the NF distribution at micrometer scale on THz photonic resonators, we now focus on smaller objects.

We performed THz s-SNOM imaging on a tuned SRR (selected in a metasurface). As for the LSA center, s-SNOM images of the SRR showed a bright and dark pattern on the arms of the device (Figure 3, b): A bright region is imaged on the N arm of the resonator (as labeled on Figure 3, b) with a local maxima located on the arm 500 nm away from the

gap edge. (C: +111 % between the N arm and the substrate). This bright region is extending into the gap (C: +23 % between the HR-Si in the gap and the surrounding substrate). As soon as the tip scans the S arm, signal vanishes and gold appears darker than silicon (C: -9 % between the S arm and the substrate). This feature is observed on images from the 1st to the 4th harmonics of Ω (Figure S3, a, b). Note that typical dark fringe artifacts are also visible on the images when the probe encounters the edges of the SRR [62], but are distinct from the described features. The topography-induced artifacts are further described in the Supporting Information (Figure S4). The AFM topography did not show any contrast between the dark and bright areas of the device (Figure 3, c). This pattern was found to be identical on every tuned SRR we scanned, independently of its location in the metasurface (Figure 3, e).

To compare with the computed NF distribution of the tuned SRR (Figure 3, a,), the maximum on the N arm is in good agreement with the FDTD simulation (Figure 3, d). However, as for the LSA, the simulation does not account for the dark area. Similar design of SRRs have been already studied by other THz microscopy techniques at larger scale [52, 53, 54, 55, 56, 57, 58, 59], but to the best of our knowledge, this feature was not previously reported and may only manifest in THz s-SNOM.

It is worth to mention that the N-S asymmetry of the SRR is the opposite of the asymmetry on the probes the LSA, *i.e.* the dark probe of the arm A is on the north while the bright probe on the arm B is on south (Figure 2, b). Therefore, the N-S asymmetries are not simply caused by a shadowing effect of the cantilever. We hypothesize that this effect is likely not limited to this two micro-resonators and requires further investigation. To explore the N-S asymmetry, we performed a series of control experiments on SRRs.

1. First, we repeated the experiment on a detuned SRR (selected in a metasurface) that is expected to show lower field concentration. The recorded s-SNOM image (Figure S5, a, b) exhibited similar N-S asymmetry, but largely attenuated (Table S2) and dominated by edge artifacts. Only the contrast in the gap is of similar amplitude than on the tuned SRR (Table S2). Therefore, this feature may not be ascribed to the photonic mode of the SRR but rather to enhanced scattering when the tip is close to the metallic edges of the structure. The main feature on the s-SNOM image of the detuned SRR is an enhanced optical contrast with respect to the substrate on the right side of the resonator (Table S2). This last result indicates that the THz s-SNOM technique allows to clearly discriminate between tuned and detuned photonic resonators.
2. We also formulated the hypothesis that the N-S asymmetry may arise from an unexpected multi-resonators effect (*e.g.* scattering of the THz beam by surrounding meta-atoms leading to interference). Such effect would have been unnoticed during the THz-TDS characterization. To verify this last point, we restarted the experiment under the same conditions but on an isolated resonator. The exact same image is obtained on the isolated SRR with the same amplitude (figure S6, a, b) and contrast (Table S2). This observation led us to exclude the contribution of any spurious lattice effect in the imaging process. The identical amplitude of the s-SNOM signal on the isolated SRR and the meta-atom indicates that when s-SNOM is performed on arrays of SRRs, only one contributes to the image formation, *i.e.*, the NF signal is not altered by the surroundings resonators.
3. We verified that N-S asymmetry did not originated from an adventitious phase contrast [63]. We compared the results obtained by HD and pseudo-heterodyne detection (PHD) (Figure S7, a-c). Amplitude images yielded the same features by HD and PHD with the same contrasts (Table S2). This observation excludes contrast on HD resulting from a phase shift between the N and S arms.
4. Influence of the substrate on the observed pattern was also excluded. THz s-SNOM images of tuned and detuned SRRs on quartz crystal substrates (α-SiO_2) assembled in metasurfaces (Figure S8, a, b, c) revealed the same features than on HR-Si (Table S2).
5. Finally, on the α-SiO_2 sample, we also excluded that the probe was responsible for the N-S asymmetry. When restarting the experiment with a different probe model (Figure S9, a, b), the same N-S asymmetry was recovered (Table S2).

This series of experiments further confirms that N-S contrast is a general feature when confined NF of THz micro-resonators are scattered during s-SNOM imaging. In the following, we discuss on the origin of this effect that requires to be elucidated for future studies.

3 Discussion

To sum up, we demonstrated the capability of the s-SNOM to recover information from THz photonic devices in the NF. For large-bandwidth LSA, local maxima of the concentrated electric field on the arms were successfully imaged. Through the study of SRRs, we demonstrated that THz s-SNOM allows to probe the NF of a single device as small as

13 µm, even if embedded in arrays. THz s-SNOM allows to discriminate efficiently tuned and detuned micro-resonators: when the incident radiation is tuned to the resonance frequency of the device, NF confinement associated to the photonic mode was recorded with a strong contrast with respect to the HR-Si substrate on the N arm. However, for both the LSA and the SRRs, an additional N-S contrast is also present on the images. At this point of our investigations, we cannot attribute the N-S contrast to any controllable parameter of the experiment. Indeed, we determined that N-S asymmetry is not specific to SRRs, does not originates from background, multi-resonators effect or phase-induced contrast. The asymetry is also clearly observed on SRRs when we replaced the HR-Si substrate with α-SiO_2 and changed the shape of the probe. Therefore, to elucidate the discrepancy between experimental data and our calculations, we focused on the explanation of this contrast through the origin of the measured s-SNOM signal.

In eq. 4 (see Methods), E_s accounts for the illumination, concentration, scattering, collection and detection of THz radiation in the probe / resonator system. Due to optical reciprocity, any requirement to illuminate the system also apply to collect the outgoing radiation. From this point of view, the bright (resp. dark) regions on our images would correspond to efficient (resp. poor) illumination and collection of light into the probe / SRR ensemble when the tip is on the N (resp. S) arm of the capacitor. We extended our calculations to reach a more realistic description of the system, now treated as a complex antenna problem. We performed broadband FDTD simulations with a conductive tip placed on several spots along the arms of a SRR (see Supporting Information). We observed a critical influence of the position of the probe on the illumination / collection pattern of the system (Figure 4, a). If placed on the N (resp. S) arm of the capacitor, a lobe oriented S (resp. N) is generated in the far-field. Previous work by Hale *et al.* with PC antenna sensors concluded that the probe is non-invasive if placed at least 10 µm above the sample [57], but in our case, the average tip-sample distance is two orders of magnitude smaller.

We now focus on the influence of the tip position on the image formation. We computed a scan line on the SRR, *i.e.*, we calculated an analogous coefficient to S_2 (see methods and SI) of the intensity received at a location similar to the position of the off-axis parabolic mirror (centered around 45° with respect to the z axis) with an approaching tip displaced from the N to the S arm (Figure 4, b). The features observed on the s-SNOM images, *i.e.* bright N arm with a local maximum and extinction of the S arm are well reproduced at the same locations. In this configuration, the illumination / collection lobe is facing the mirror when the tip is on the N arm, but is oriented backward when the tip is on on the S arm (Figure 4, c). At this point of our investigations, this scenario agrees well with the experimental data. We consider the interplay between the confined NF, its multiplication with the FF illumination / collection pattern, and the aperture-limited focusing optics as a strong contribution to the recorded images (N.A. = 0.39 in our case, according to the manufacturer information).

It is known that the probe shape and oscillations contributes to the contrast of THz s-SNOM images [23]. Our results indicates that the collection mirror also participates to the contrast if the tip-sample ensemble has an anisotropic FF pattern. Therefore, within most of s-SNOM apparatuses with a mirror in front of the probe, the lobe pointing north would not be accessible. Acuna *et al.*[58] used a technique similar to s-SNOM on SRRs but did not report this effect. However, in this study, a broadband THz source was used and authors attributed the image contrast to both the fundamental mode and surface plasmons polaritons. We demonstrated that the tip presence perturbs the photonic mode in a way that the symmetry of the device is broken. The classic picture of (Figure 1, b) should evolve towards the one of (Figure 4, c).

In this framework, for a photonic resonator located at a position (x, y, z) with respect to the tip and the mirror, and oriented with an angle ψ in the sample plane, the scattered NF contains information on both the spatial distribution of the photonic mode, labeled here as $\mathrm{NF}(x, y, z)$ and the FF pattern that is modified by the tip, labeled here as $\mathrm{FF}(x, y, z, \theta, \varphi, \psi)$, limited by the portion of solid angle where the FF pattern is collected. In our case, this last is defined by the numerical aperture of the mirror. One can then write the problem as eq. 2, for a monochromatic incident wave with a given linear polarization. Note that the NF and FF terms in eq. 2 are squared since they intervene both in illumination and collection. It is also worth to mention that a more sophisticated description should integrate the scattering efficiency of the probe and the dielectric properties of the material beneath that still account for s-SNOM signal.

$$E_s(x, y, z) \propto \iint_{\text{mirror}} \mathrm{NF}^2(x, y, z)\mathrm{FF}^2(x, y, z, \theta, \varphi, \psi) d\theta d\phi. \tag{2}$$

So far, we cannot overcome this issue with current microscope designs that would requires to replace the parabolic mirror by a Cassegrain reflector or to rotate the mirror during the scan. However, if the mirror cannot rotate, it is possible in some particular cases to rotate the sample.

We scanned tuned SRRs on HR-Si oriented by $\psi = -45°, 0°, 45°$ and $90°$, ψ being defined in Figure 5, a. The contribution of the illumination / collection lobes is further evidenced on the obtained images that are in good agreement

with our scenario (Figure 5, a): for $\psi = -45°, 0°$ and $+45°$ the N-S asymmetry is pronounced since the mirror captures part of a lobe when the tip is on the N arm. For $\psi = 90°$ smaller signals are detected and the region of the arms is less asymmetric since the lobe is oriented parallel to the mirror.

We also note that the extension of the bright regions on the SRRs is not the same for each angle since the N and S directions are defined in the frame of reference of the SRR, labeled as (x', y'), but not in the laboratory one, noted here (x, y), the respective slow and fast scan axis of the AFM. We used the orientation-dependent detection of the pattern to reconstruct the NF of the SRR by numerical methods from the four obtained images.

First, we rotated the images to handle the data in the coordinates of the SRR noted hereafter $f(x', y')$. Secondly, we computed the symmetric and asymmetric parts of each image, respectively $\frac{1}{2}(f(x', y') + f(-x', -y'))$ and $\frac{1}{2}(f(x', y') + f(-x', -y'))$ and filtered the asymmetric part. The symmetrization is here equivalent to an experiment where another parabolic mirror would be placed on the head of the AFM, which is not technically feasible. Finally, we summed the symmetrized images, as if 8 mirrors were in the apparatus to simultaneously inject and detect THz light on the tip / SRR ensemble. Despite being rather trivial, this method allows to recover almost the whole signal on the entire half space. The reconstructed image (Figure 5, b, c) show the expected attributes, *i.e.*, bright N and S arms with local maxima resulting from the localized E field of the photonic mode, in good agreement with the computed NF distribution (Figure 3, a).

Note that this method is only applicable to resonators with planes of symmetry and therefore cannot be applied to the LSA. In addition, the reconstruction procedure is found to enhance edge artifacts and the line defects, *i.e.* the shift between lines, are now in 4 directions after rotation. It is also worth to mention that the artificial increase of the numerical aperture may not fully capture all the FF pattern, especially if pointing vertically. Ideally, a practical way to circumvent the NF / FF multiplication leading to complex patterns for asymmetric systems would be to separate the illumination and collection of light in s-SNOM apparatus.

4 Conclusions

Throughout this work, we investigated the NF confinement associated to the photonic mode of THz resonators by s-SNOM. We imaged NF in broadband LSA and tuned SRR, the last being only 13 µm large with arms as small as 2 µm ($\sim \lambda/60$). Note that this smallest feature of the SRR is two orders of magnitude larger than accessible THz s-SNOM resolution and that smaller objects on the SRR can, in principle, be coupled to the SRR and imaged by s-SNOM.

Indeed, the bright regions imaged on photonic micro-resonators with strong E-field concentration can be used on template substrates as additional local field concentrators to improve the performance of s-SNOM imaging of micro or nano objects. For instance, a few bio-macromolecules deposited on a tuned SRR could be imaged with high sensitivity on the N arm.

Nonetheless, the recorded images also showed unexpected asymmetric features. We interpreted this effect on the basis of numerical calculations as NF / FF multiplication leading to the illumination and collection of light in the system to be highly dependent on the position of the tip on the resonator. We emphasize that interpretation of THz s-SNOM images of structures radiating electric field is non-trivial. In other words, scanning a micro-antenna-like device with a micro-antenna-like scattering tip must be treated as a sophisticated macro-antenna problem. By numerical image reconstruction, the NF / FF multiplication can be eliminated but this operation is only applicable to objects with planes of symmetry that can be rotated in the microscope.

In principle, NF imaging free of spatial FF multiplication should be accessible with future s-SNOM designs where incident and detected scattered light do not follow the same path[64].

5 Methods

5.1 FDTD computations

All the simulations were performed with the FDTD software from Lumerical. Computations without probe, *i.e.*, transmission spectra and NF distribution, are obtained with periodic boundary condition and plane wave excitation at normal incidence, with the SRRs and LSA on an infinitely thick substrate to avoid Fabry-Pérot effect. For the LSA (resp. SRRs), polarization of the incident wave is collinear with the probes of the LSA (resp. the arms of the SRRs). Computations with a probe on the micro-resonator required to avoid artifact from the FF projection from truncated data. The FF radiation patterns are then calculated from the field on a closed box enclosing the SRR and the s-SNOM probe. Because the refractive index along this box needs to be uniform, those simulation are run without substrate. The SRR is excited with a TFSF (Total-Field, Scattered-Field) source inside the box, and we use Perfect Matching Layer (PML)

boundary condition in every direction. Reflection of the incident wave on the sample was numerically subtracted to retain only the scattered field. The tip was modeled as a truncated square-base pyramid (69.7 µm long and respectively 10.5 and 0.2 µm for the base and the apex side lengths).

To compute a scan line, the scattering radiation pattern of the SRR and the tip is simulated for 20 positions of the tip along the N-S axis, and 4 positions along the z-axis, *i.e.*, 80 simulations overall. The computed 2Ω coefficient of the intensity, that is analogous to the amplitude of the demodulated intensity at the 2nd harmonic of the tip oscillation in the experiment, is calculated from the 4 positions along the z-axis. Additional details are given in the Supporting Information.

5.2 Manufacturing of the devices

The micro-resonators are made of gold on 300-µm-thick HR-Si ($> 10\,\mathrm{k\Omega cm}$) substrates, provided by Sil'tronix, following standard electron beam lithography process: i) Cleaning of the HR-Si using piranha solution to ensure a good hydroxylation of the surface and thus a good adhesion of the resist. ii) Coating with a double positive resist layer (Poly (methyl methacrylate), PMMA). iii) Deposition of a conductive resist layer. iv) Electron beam writing of the micro-resonators and resist development. v) Deposition of a 20 nm thick titanium layer for the adhesion followed by a 200 nm thick gold layer. vi) Lift-off of the remaining resist to keep only the micro-resonators.

The resonators in this study are LSAs in metasurfaces (2.2 x 2.2 mm, 150 µm periodicity), tuned and detuned SRRs in metasurfaces (2.2 x 2.2 mm, 50 µm periodicity) and tuned isolated SRRs, with the same orientation than the SRRs in the metasurfaces or tilted by an angle ψ of -45°, 45° and 90°.

5.3 THz-TDS

The THz TDS was carried out using a commercial apparatus Terasmart (MenloSystems) placed in a glovebox purged with dry-nitrogen to avoid absorption from water vapor. The procedure is described elsewhere [12].

5.4 THz s-SNOM

We performed s-SNOM imaging using a NeaSNOM microscope (Neaspec). The THz source is a CO_2 pumped methanol gas laser (FIRL-100, Edinburgh Instruments) emitting at 2.522 THz (continuous wave). At the entrance of the integrated interferometer of the microscope, we measured typical constant optical power during a scan between 20 and 40 mW. The output optical signal of the microscope is detected with a pulse-tube-cooled InSb hot electron bolometer (QMC Instruments).

In the HD scheme, intensity received by the detector and demodulated at $n\Omega$ (I_n) can be expressed as eq. 3

$$I_n = |E_s|^2 + 2|E_s||E_{bg}|\cos(\phi_s - \phi_{bg}) + 2|E_s||E_R|\cos(\phi_s - \phi_R), \tag{3}$$

ϕ_S, ϕ_{bg} and ϕ_R being the respective phases of the scattered NF, the background and the reference beam. Eq. 1 can be approximated as eq. 4, provided that $|E_R| >> |E_{bg}|$:

$$I_n \approx 2|E_s||E_R|\cos(\phi_s - \phi_R). \tag{4}$$

We used probes with elongated (70 µm) Pt coated Si tips ($\Omega = 280\,\mathrm{kHz}$) designed for efficient scattering of THz radiation (Lprobes, Vmicro). Note that the positions of all the components of the microscope are fixed once the beam is focused on the tip apex and that only the sample moves during the scan. The recorded images are show with a linear false-color scale excluding outlying pixels for the sake of clarity. We show laterally averaged sections of the images along an arbitrary axis (d) to discuss the observed features. Dimensions of the images and the width of the lateral averaging of the sections are given in the Supplementary Information (Table S1). Additional details are given in the Supporting Information.

6 Acknowledgement

This work was supported by the joint lab LabCom Horiba-IEMN, the international chair of excellence "ThOTroV" from region "Hauts-de-France", the welcome talent grant "NeFiStoV" from the European Metropole of Lille (MEL), the I-site ULNE through "TeraStoVe" pluridisciplinary project, the National Research Agency (ANR) under programs "ExCELSiOR" ANR 11-EQPX-0015 and "COMI", ANR-17-CE24-0002, and the French RENATECH network on micro and nanotechnologies.

7 Conflicts of interest

B. W. and M. F. are respectively CEO and co-founder of Vmicro SAS, a company manufacturing and commercializing AFM probes, including the Lprobes used in this study. Other authors do not declare competing financial interests.

8 Authors contributions

L. T., T. H. and C. N. S. contributed equally to this work. The s-SNOM experiments were performed by C. N. S. and L. T. with the help of S. E. and B. W. T. H. performed the calculations by FDTD, the sample fabrication and the optical design of the setup. Characterization by THz-TDS was performed by M. L. and T. H. The work of T. H. and M. L. was done as a part of their doctoral studies under the supervision of R. P. and J.-F. L. The project was conceived by R. P. and managed with the help of J.-F. L. and M. F. The paper was written by L. T. with inputs from all the authors.

9 Supplementary Material

Additional methods and materials including: details on the computation of the S_2 analogous, details on the s-SNOM experiments, the transmission of the micro-resonators (computed and probed by THz-TDS) and a commented section along the arms of a SRR. Additional s-SNOM images: On HR-SI: S_n (n = 1 - 4) for a LSA and a SRR, and S_2 for a detuned SRR, an isolated tuned SRR (HD and PHD). On α-SiO_2: S_2 for a tuned SRR imaged with long and short probes.

10 Bibliography

References

[1] Robert E Miles, X-C Zhang, Heribert Eisele, and Arunas Krotkus. *Terahertz frequency detection and identification of materials and objects*. Springer Science & Business Media, 2007.

[2] Michael C. Kemp, P. F. Taday, Bryan E. Cole, J. A. Cluff, Anthony J. Fitzgerald, and William R. Tribe. Security applications of terahertz technology. In R. Jennifer Hwu and Dwight L. Woolard, editors, *Terahertz for Military and Security Applications*, volume Proc. SPIE 5070, page 44, Orlando, FL, August 2003.

[3] Erik Bründermann, Heinz-Wilhelm Hübers, and Maurice FitzGerald Kimmitt. *Terahertz Techniques*. Springer Berlin Heidelberg, 2012.

[4] Wai Lam Chan, Jason Deibel, and Daniel M Mittleman. Imaging with terahertz radiation. *Reports on Progress in Physics*, 70(8):1325–1379, August 2007.

[5] Tao Chen, Suyan Li, and Hui Sun. Metamaterials Application in Sensing. *Sensors*, 12(3):2742–2765, February 2012.

[6] Romain Peretti, Flavie Braud, Emilien Peytavit, Emmanuel Dubois, and Jean-François Lampin. Broadband Terahertz Light–Matter Interaction Enhancement for Precise Spectroscopy of Thin Films and Micro-Samples. *Photonics*, 5(2):11, May 2018.

[7] S J Park, J T Hong, S J Choi, H S Kim, W K Park, S T Han, J Y Park, S Lee, D S Kim, and Y H Ahn. Detection of microorganisms using terahertz metamaterials. *Scientific Reports*, 4(4988):7, May 2014.

[8] Riccardo Degl'Innocenti, David S. Jessop, Yash D. Shah, Juraj Sibik, J. Axel Zeitler, Piran R. Kidambi, Stephan Hofmann, Harvey E. Beere, and David A. Ritchie. Low-Bias Terahertz Amplitude Modulator Based on Split-Ring Resonators and Graphene. *ACS Nano*, 8(3):2548–2554, March 2014.

[9] Curdin Maissen, Giacomo Scalari, Federico Valmorra, Sara Cibella, Roberto Leoni, Christian Reichl, Christohpe Charpentier, Werner Wegscheider, Mattias Beck, and Jérôme Faist. Ultrastrong Coupling in the Near-field of Complementary Split Ring Resonators. *Physical Review B*, 90(20):205309, November 2014.

[10] Shuo Liu, Ahsan Noor, Liang Liang Du, Lei Zhang, Quan Xu, Kang Luan, Tian Qi Wang, Zhen Tian, Wen Xuan Tang, Jia Guang Han, Wei Li Zhang, Xiao Yang Zhou, Qiang Cheng, and Tie Jun Cui. Anomalous Refraction and Nondiffractive Bessel-Beam Generation of Terahertz Waves through Transmission-Type Coding Metasurfaces. *ACS Photonics*, 3(10):1968–1977, October 2016.

[11] K. Meng, S. J. Park, A. D. Burnett, T. Gill, C. D. Wood, M. Rosamond, L. H. Li, L. Chen, D. R. Bacon, J. R. Freeman, P. Dean, Y. H. Ahn, E. H. Linfield, A. G. Davies, and J. E. Cunningham. Increasing the sensitivity of

terahertz split ring resonator metamaterials for dielectric sensing by localized substrate etching. *Optics Express*, 27(16):23164, August 2019.

[12] R. Peretti, S. Mitryukovskiy, K. Froberger, A. Mebarki, S. Eliet, M. Vanwolleghem, and J. Lampin. THz-TDS time-trace analysis for the extraction of material and metamaterial parameters. *IEEE Transactions on Terahertz Science and Technology*, pages 1–1, 2018.

[13] George Keiser and Pernille Klarskov. Terahertz Field Confinement in Nonlinear Metamaterials and Near-Field Imaging. *Photonics*, 6(1):22, February 2019.

[14] Hironaru Murakami, Naotsugu Uchida, Ryotaro Inoue, Sunmi Kim, Toshihiko Kiwa, and Masayoshi Tonouchi. Laser Terahertz Emission Microscope. *Proceedings of the IEEE*, 95(8):1646–1657, August 2007.

[15] O. Mitrofanov, M. Lee, J.W.P. Hsu, I. Brener, R. Harel, J.F. Federici, J.D. Wynn, L.N. Pfeiffer, and K.W. West. Collection-mode near-field imaging with 0.5-THz pulses. *IEEE Journal of Selected Topics in Quantum Electronics*, 7(4):600–607, September 2001.

[16] Markus Wächter, Michael Nagel, and Heinrich Kurz. Tapered photoconductive terahertz field probe tip with subwavelength spatial resolution. *Applied Physics Letters*, 95(4):041112, July 2009.

[17] Andreas Bitzer, Alex Ortner, and Markus Walther. Terahertz near-field microscopy with subwavelength spatial resolution based on photoconductive antennas. *Applied Optics*, 49(19):E1, July 2010.

[18] M. A. Seo, A. J. L. Adam, J. H. Kang, J. W. Lee, S. C. Jeoung, Q. H. Park, P. C. M. Planken, and D. S. Kim. Fourier-transform terahertz near-field imaging of one-dimensional slit arrays: mapping of electric-field-, magnetic-field-, and Poynting vectors. *Optics Express*, 15(19):11781, September 2007.

[19] N. Klein, P. Lahl, U. Poppe, F. Kadlec, and P. Kužel. A metal-dielectric antenna for terahertz near-field imaging. *Journal of Applied Physics*, 98(1):014910, July 2005.

[20] S Hunsche, M Koch, I Brener, and M.C Nuss. THz near-field imaging. *Optics Communications*, 150(1-6):22–26, May 1998.

[21] Hou-Tong Chen, Roland Kersting, and Gyu Cheon Cho. Terahertz imaging with nanometer resolution. *Applied Physics Letters*, 83(15):3009–3011, October 2003.

[22] F. Blanchard, A. Doi, T. Tanaka, H. Hirori, H. Tanaka, Y. Kadoya, and K. Tanaka. Real-time terahertz near-field microscope. *Optics Express*, 19(9):8277, April 2011.

[23] Curdin Maissen, Shu Chen, Elizaveta Nikulina, Alexander Govyadinov, and Rainer Hillenbrand. Probes for Ultrasensitive THz Nanoscopy. *ACS Photonics*, 6(5):1279–1288, May 2019.

[24] Xinzhong Chen, Debo Hu, Ryan Mescall, Guanjun You, D. N. Basov, Qing Dai, and Mengkun Liu. Modern Scattering-Type Scanning Near-Field Optical Microscopy for Advanced Material Research. *Advanced Materials*, 31(24):1804774, 2019.

[25] Y. De Wilde, F. Formanek, and L. Aigouy. Apertureless near-field scanning optical microscope based on a quartz tuning fork. *Review of Scientific Instruments*, 74(8):3889–3891, aug 2003.

[26] Fritz Keilmann and Rainer Hillenbrand. Near-field microscopy by elastic light scattering from a tip. *Philosophical Transactions of the Royal Society of London. Series A: Mathematical, Physical and Engineering Sciences*, 362(1817):787–805, apr 2004.

[27] A. J. Huber, F. Keilmann, J. Wittborn, J. Aizpurua, and R. Hillenbrand. Terahertz Near-Field Nanoscopy of Mobile Carriers in Single Semiconductor Nanodevices. *Nano Letters*, 8(11):3766–3770, November 2008.

[28] Rainer Jacob, Stephan Winnerl, Markus Fehrenbacher, Jayeeta Bhattacharyya, Harald Schneider, Marc Tobias Wenzel, Hans-Georg von Ribbeck, Lukas M. Eng, Paola Atkinson, Oliver G. Schmidt, and Manfred Helm. Intersublevel Spectroscopy on Single InAs-Quantum Dots by Terahertz Near-Field Microscopy. *Nano Letters*, 12(8):4336–4340, August 2012.

[29] Clemens Liewald, Stefan Mastel, Jeffrey Hesler, Andreas J. Huber, Rainer Hillenbrand, and Fritz Keilmann. All-electronic terahertz nanoscopy. *Optica*, 5(2):159, February 2018.

[30] Jiawei Zhang, Xinzhong Chen, Scott Mills, Thomas Ciavatti, Ziheng Yao, Ryan Mescall, Hai Hu, Vyacheslav Semenenko, Zhe Fei, Hua Li, Vasili Perebeinos, Hu Tao, Qing Dai, Xu Du, and Mengkun Liu. Terahertz Nanoimaging of Graphene. *ACS Photonics*, 5(7):2645–2651, July 2018.

[31] H. T. Stinson, A. Sternbach, O. Najera, R. Jing, A. S. Mcleod, T. V. Slusar, A. Mueller, L. Anderegg, H. T. Kim, M. Rozenberg, and D. N. Basov. Imaging the nanoscale phase separation in vanadium dioxide thin films at terahertz frequencies. *Nature Communications*, 9(1), December 2018.

[32] Ziheng Yao, Vyacheslav Semenenko, Jiawei Zhang, Xiaoguang Zhao, Xinzhong Chen, Hai Hu, Ryan Mescall, Thomas Ciavatti, Stephen March, Seth R Bank, Tiger H Tao, Xin Zhang, Vasili Perebeinos, Qing Dai, and Xu Du. Photo-induced terahertz near-field dynamics of graphene/InAs heterostructures. *Optics Express*, 27(10):13611–13622, 2019.

[33] Amin Soltani, Frederik Kuschewski, Marlene Bonmann, Andrey Generalov, Andrei Vorobiev, Florian Ludwig, Matthias M. Wiecha, Dovilė Čibiraitė, Frederik Walla, Stephan Winnerl, Susanne C. Kehr, Lukas M. Eng, Jan Stake, and Hartmut G. Roskos. Direct nanoscopic observation of plasma waves in the channel of a graphene field-effect transistor. *Light: Science & Applications*, 9(1), December 2020.

[34] Chao Chen, Shu Chen, Thomas Taubner, Wei Xiong, Ming Xu, Xinliang Zhang, Xiangshui Miao, Peining Li, and Rainer Hillenbrand. Terahertz Nanoimaging and Nanospectroscopy of Chalcogenide Phase-Change Materials. *ACS Photonics*, 7(12):3499–3506, 2020.

[35] Thales V. A. G. de Oliveira, Tobias Nörenberg, Gonzalo Álvarez-Pérez, Lukas Wehmeier, Javier Taboada-Gutiérrez, Maximilian Obst, Franz Hempel, Eduardo J. H. Lee, J. Michael Klopf, Ion Errea, Alexey Y. Nikitin, Susanne C. Kehr, Pablo Alonso-González, and Lukas M. Eng. Nanoscale-Confined Terahertz Polaritons in a van der Waals Crystal. *Advanced Materials*, 33(2):2005777, 2021.

[36] Kiwon Moon, Youngwoong Do, Hongkyu Park, Jeonghoi Kim, Hyuna Kang, Gyuseok Lee, Jin-Ha Lim, Jin-Woo Kim, and Haewook Han. Computed terahertz near-field mapping of molecular resonances of lactose stereo-isomer impurities with sub-attomole sensitivity. *Scientific Reports*, 9(1), December 2019.

[37] Stephan Schäffer, Anna Katharina Wigger, and Peter Haring Bolívar. Substrate-enhanced THz nanoscopic recognition of single bacteria. In *2019 44th International Conference on Infrared, Millimeter, and Terahertz Waves (IRMMW-THz)*, pages 1–2, September 2019. ISSN: 2162-2027.

[38] Zhongbo Yang, Dongyun Tang, Jiao Hu, Mingjie Tang, Mingkun Zhang, Hong-Liang Cui, Lihua Wang, Chao Chang, Chunhai Fan, Jiang Li, and Huabin Wang. Near-Field Nanoscopic Terahertz Imaging of Single Proteins. *Small*, page 2005814, December 2020.

[39] Kiwon Moon, Hongkyu Park, Jeonghoi Kim, Youngwoong Do, Soonsung Lee, Gyuseok Lee, Hyeona Kang, and Haewook Han. Subsurface Nanoimaging by Broadband Terahertz Pulse Near-Field Microscopy. *Nano Letters*, 15(1):549–552, January 2015.

[40] F. Kuschewski, H.-G. von Ribbeck, J. Döring, S. Winnerl, L. M. Eng, and S. C. Kehr. Narrow-band near-field nanoscopy in the spectral range from 1.3 to 8.5 THz. *Applied Physics Letters*, 108(11):113102, March 2016.

[41] Xinzhong Chen, Xiao Liu, Xiangdong Guo, Shu Chen, Hai Hu, Elizaveta Nikulina, Xinlin Ye, Ziheng Yao, Hans A. Bechtel, Michael C. Martin, G. Lawrence Carr, Qing Dai, Songlin Zhuang, Qing Hu, Yiming Zhu, Rainer Hillenbrand, Mengkun Liu, and Guanjun You. Thz near-field imaging of extreme subwavelength metal structures. *ACS Photonics*, 7(3):687–694, February 2020.

[42] Angela Pizzuto, Xinzhong Chen, Hai Hu, Qing Dai, Mengkun Liu, and Daniel M. Mittleman. Anomalous contrast in broadband THz near-field imaging of gold microstructures. *Optics Express*, 29(10):15190, May 2021.

[43] Riccardo Degl'Innocenti, Robert Wallis, Binbin Wei, Long Xiao, Stephen J. Kindness, Oleg Mitrofanov, Philipp Braeuninger-Weimer, Stephan Hofmann, Harvey E. Beere, and David A. Ritchie. Terahertz Nanoscopy of Plasmonic Resonances with a Quantum Cascade Laser. *ACS Photonics*, 4(9):2150–2157, September 2017.

[44] T. Zentgraf, J. Dorfmüller, C. Rockstuhl, C. Etrich, R. Vogelgesang, K. Kern, T. Pertsch, F. Lederer, and H. Giessen. Amplitude- and phase-resolved optical near fields of split-ring-resonator-based metamaterials. *Optics Letters*, 33(8):848, April 2008.

[45] Robert L. Olmon, Peter M. Krenz, Andrew C. Jones, Glenn D. Boreman, and Markus B. Raschke. Near-field imaging of optical antenna modes in the mid-infrared. *Optics Express*, 16(25):20295, December 2008.

[46] M. Schnell, A. Garcia-Etxarri, J. Alkorta, J. Aizpurua, and R. Hillenbrand. Phase-Resolved Mapping of the Near-Field Vector and Polarization State in Nanoscale Antenna Gaps. *Nano Letters*, 10(9):3524–3528, September 2010.

[47] Tomáš Neuman, Pablo Alonso-González, Aitzol Garcia-Etxarri, Martin Schnell, Rainer Hillenbrand, and Javier Aizpurua. Mapping the near fields of plasmonic nanoantennas by scattering-type scanning near-field optical microscopy. *Laser & Photonics Reviews*, 9(6):637–649, 2015.

[48] A. B. Khanikaev, N. Arju, Z. Fan, D. Purtseladze, F. Lu, J. Lee, P. Sarriugarte, M. Schnell, R. Hillenbrand, M. A. Belkin, and G. Shvets. Experimental demonstration of the microscopic origin of circular dichroism in two-dimensional metamaterials. *Nature Communications*, 7(1), November 2016.

[49] M. Schnell, P. Sarriugarte, T. Neuman, A. B. Khanikaev, G. Shvets, J. Aizpurua, and R. Hillenbrand. Real-Space Mapping of the Chiral Near-Field Distributions in Spiral Antennas and Planar Metasurfaces. *Nano Letters*, 16:663–670, January 2016.

[50] Takuya Okamoto, Toshio Sugaya, Naoki Fujimura, Kou Ishikawa, and Yukio Kawano. Near-field infrared investigations of an arm-terminated spiral structure with bow-tie probe. *Journal of Physics Communications*, 2(10):105004, October 2018.

[51] Lulu Chen, Liaoxin Sun, Hongxing Dong, Nanli Mou, Yaqiang Zhang, Qisong Li, Xiongwei Jiang, and Long Zhang. Near-field imaging of the multi-resonant mode induced broadband tunable metamaterial absorber. *RSC Advances*, 10(9):5146–5151, 2020.

[52] Andreas Bitzer, Hannes Merbold, Andreas Thoman, Thomas Feurer, Hanspeter Helm, and Markus Walther. Terahertz near-field imaging of electric and magnetic resonances of a planar metamaterial. *Optics Express*, 17(5):3826, March 2009.

[53] Andreas Bitzer, Alex Ortner, Hannes Merbold, Thomas Feurer, and Markus Walther. Terahertz near-field microscopy of complementary planar metamaterials: Babinet's principle. *Optics Express*, 19(3):2537, January 2011.

[54] Hannes Merbold, Andreas Bitzer, and Thomas Feurer. Near-field investigation of induced transparency in similarly oriented double split-ring resonators. *Optics Letters*, 36(9):1683, May 2011.

[55] Jan Wallauer, Andreas Bitzer, Stefan Waselikowski, and Markus Walther. Near-field signature of electromagnetic coupling in metamaterial arrays: a terahertz microscopy study. *Optics Express*, 19(18):17283, August 2011.

[56] Jan Wallauer, Christian Grumber, and Markus Walther. Mapping the coupling between a photo-induced local dipole and the eigenmodes of a terahertz metamaterial. *Optics Letters*, 39(21):6138, November 2014.

[57] Lucy L. Hale, Janine Keller, Thomas Siday, Rodolfo I. Hermans, Johannes Haase, John L. Reno, Igal Brener, Giacomo Scalari, Jérôme Faist, and Oleg Mitrofanov. Noninvasive Near-Field Spectroscopy of Single Subwavelength Complementary Resonators. *Laser & Photonics Reviews*, 14(4):1900254, 2020. Number: 4.

[58] G. Acuna, S. F. Heucke, F. Kuchler, H. T. Chen, A. J. Taylor, and R. Kersting. Surface plasmons in terahertz metamaterials. *Optics Express*, 16(23):18745, November 2008.

[59] F. Blanchard, K. Ooi, T. Tanaka, A. Doi, and K. Tanaka. Terahertz spectroscopy of the reactive and radiative near-field zones of split ring resonator. *Optics Express*, 20(17):19395, August 2012.

[60] L Aigouy, A Lahrech, S Gresillon, H Cory, A C Boccara, and J C Rivoal. Polarization effects in apertureless scanning near-field optical microscopy: an experimental study. *Optics Letters*, 24(4):3, February 1999.

[61] Rebecca Büchner, Thomas Weber, Lucca Kühner, Stefan A. Maier, and Andreas Tittl. Tip Coupling and Array Effects of Gold Nanoantennas in Near-Field Microscopy. *ACS Photonics*, page 3486–3494, October 2021.

[62] V. E. Babicheva, S. Gamage, M. I. Stockman, and Y. Abate. Near-field edge fringes at sharp material boundaries. *Optics Express*, 25(20):23935, October 2017.

[63] Nenad Ocelic, Andreas Huber, and Rainer Hillenbrand. Pseudoheterodyne detection for background-free near-field spectroscopy. *Applied Physics Letters*, 89(10):101124, September 2006.

[64] Susana Moreno-Flores and Jose L. Toca-Herrera. *Hybridizing Surface Probe Microscopies*. CRC Press, nov 2012.

11 Figures

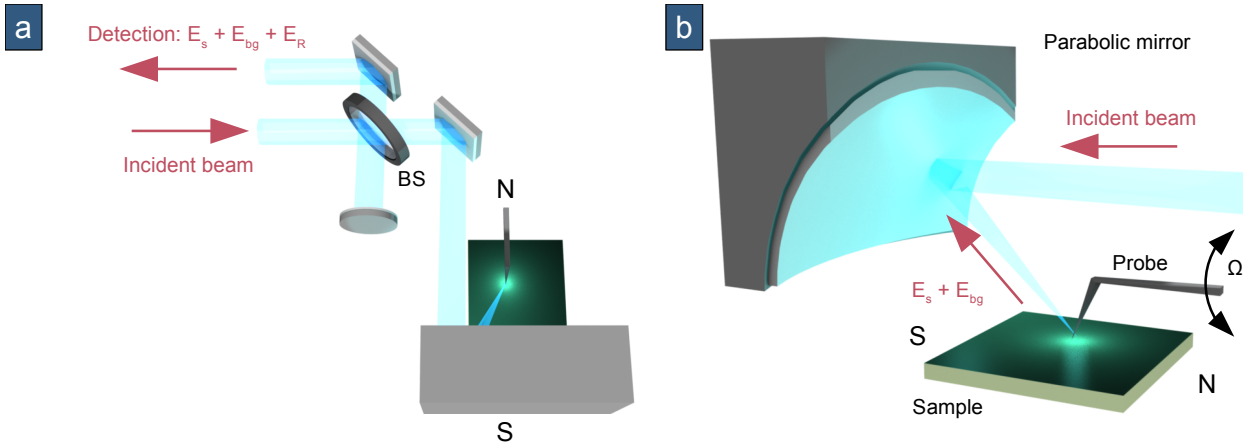

Figure 1: **Schematic representation of the s-SNOM setup (not to scale). (a):** The beam of a CO_2-pumped methanol gas laser enters the interferometer of the microscope and is focused by a parabolic mirror on the tip in intermittent contact with the sample. The parabolic mirror also collect the scattered NF and the adventitious background. Optical signals are combined with the reference arm of the interferometer and detected by an InSb hot electrons bolometer. **(b):** Side view of the parabolic mirror, the probe and the sample.

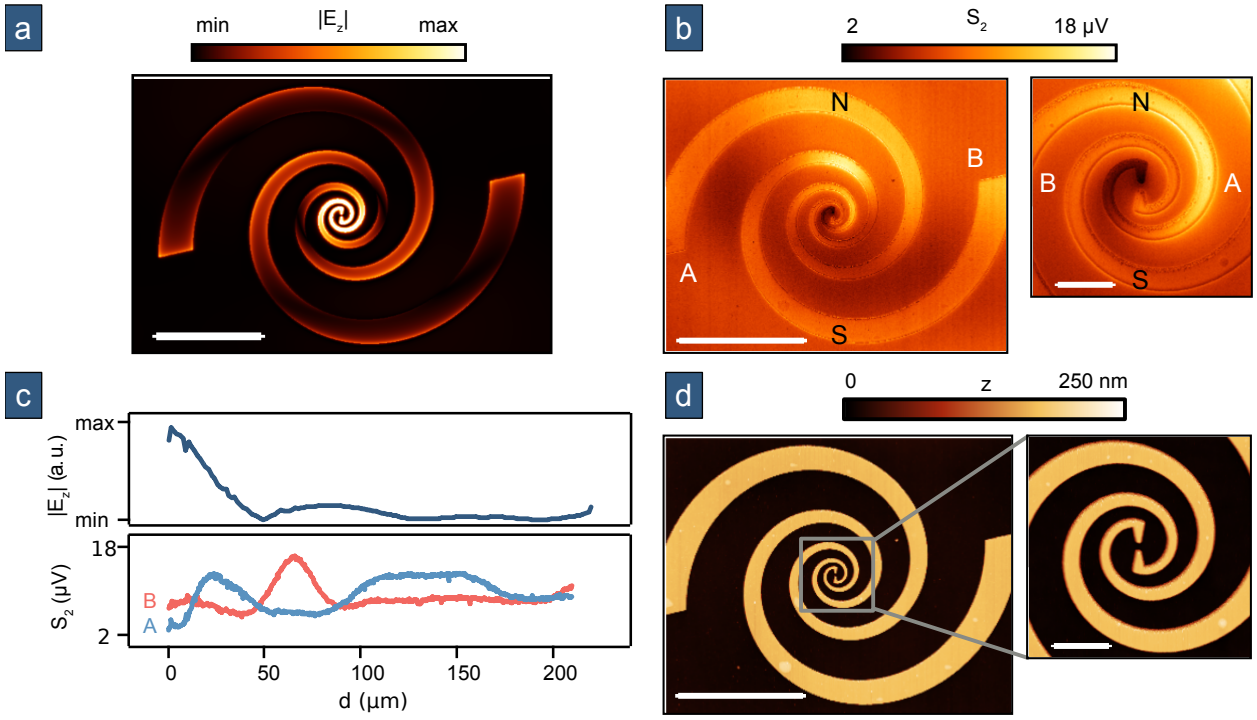

Figure 2: **NF distribution on a LSA : (a)**: Computed NF ($|E_z|^2$) on a LSA, scale bar length is 30 μm. **(b):** s-SNOM images of an LSA: Left panel: large scale scan, scale bar length is 30 μm. Right panel: detail of the center, scale bar length is 5 μm. **(c)** Top panel: Section along an arm of LSA in (a) (both arms give the same curve). Bottom panel: Mean sections along the arms of the LSA on (b). Blue line: arm A, red line: arm B. Origin is the apex of the probe of the bowtie. **(d):** Respective topographies measured simultaneously with (b).

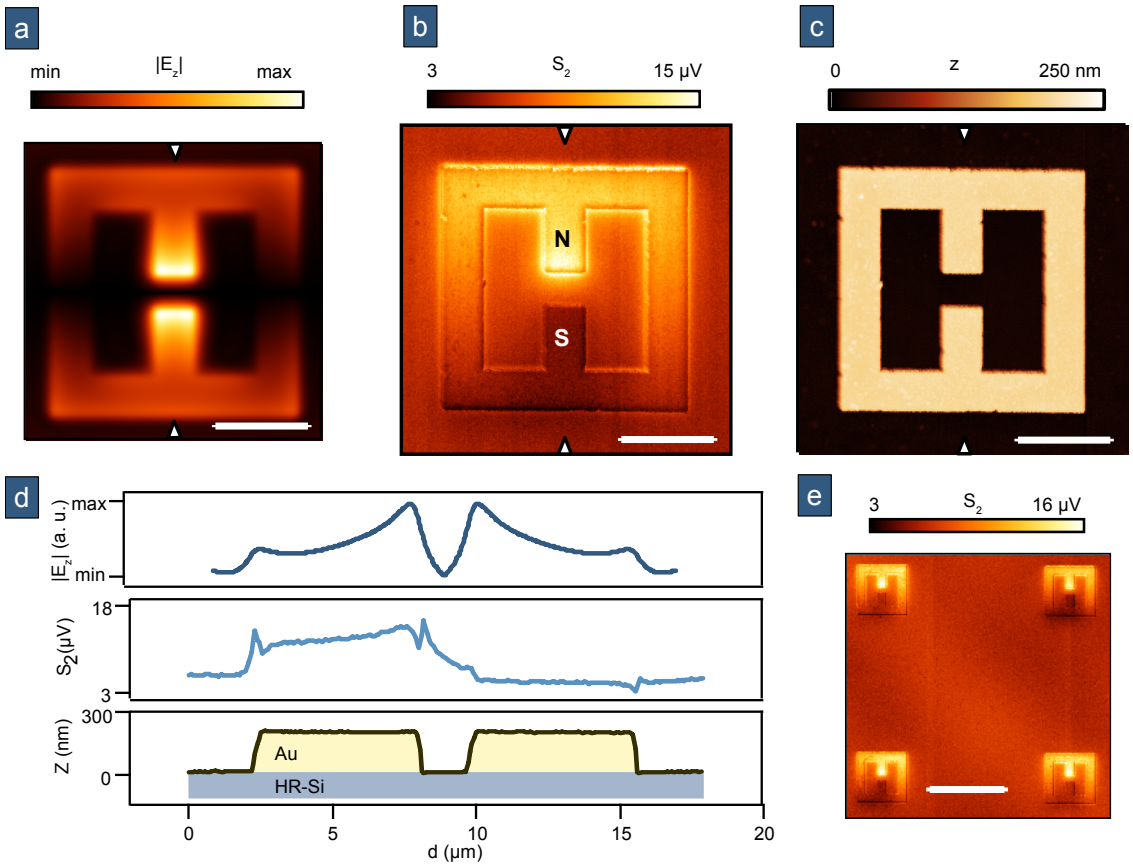

Figure 3: **NF distribution on tuned SRRs: (a):** Computed NF ($|E_z|^2$) of a tuned SRR (l = 13 µm, g = 2 µm), scale bar length is 5 µm. **(b):** s-SNOM image of a tuned SRR (l = 13 µm, g = 2 µm), scale bar length is 5 µm. **(c):** Respective topography. **(d):** Top panel: Section of the computed NF along the triangular symbols on (a). Center panel: Mean section between triangular symbols on (b). Bottom panel: Mean section (6 px) between triangular symbols on (c). **(e):** s-SNOM image of four adjacent tuned SRRs, scale bar length is 20 µm.

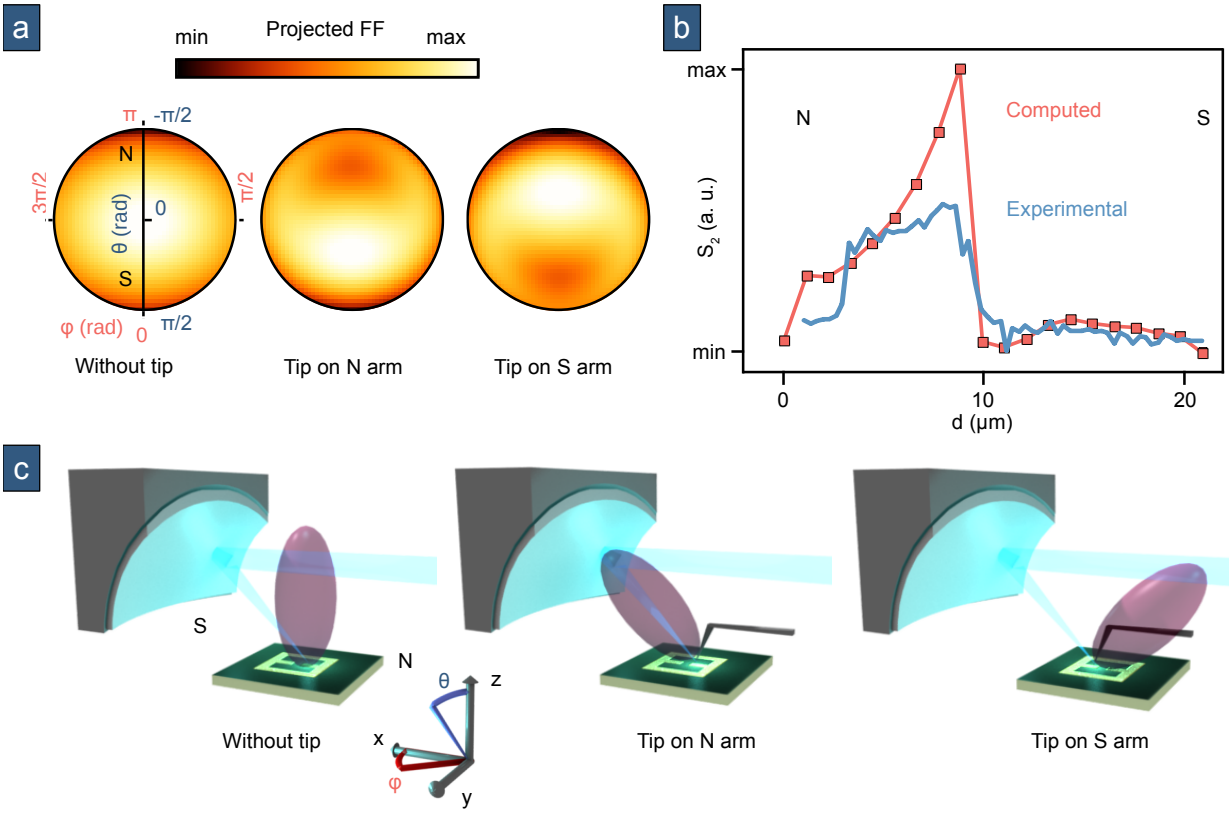

Figure 4: **Tip / resonator modelling reveals a strongly asymmetrical illumination / collection FF pattern that accounts for the asymmetrical s-SNOM images : (a):** Computed FF emission pattern, polar projected, viewed from top. From left to right: when no tip is on the SRR, when a tip scans the N arm, when a tip contacts the S arm. **(b):** Red line: computed scan line, blue line: experimental data. **(c):** Schematic representation (not to scale) of the illumination / collection lobes within the microscope. From left to right: when no tip is on the SRR, when a tip contacts the N arm, when a tip contacts the S arm.

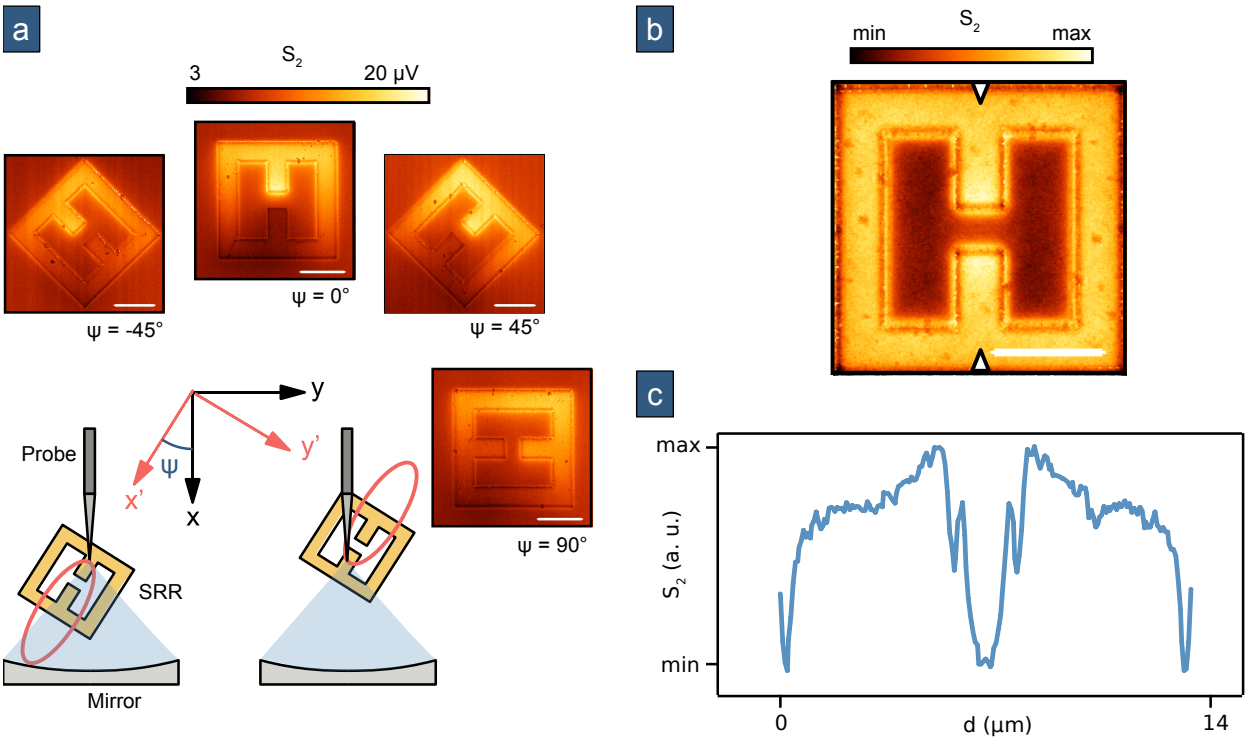

Figure 5: **The asymmetry shown for different orientations and image reconstruction : (a):** THz s-SNOM images of tuned SRRs (l = 13 µm, g = 2 µm) oriented at $\psi = -45°, 0°, 45°$ and $90°$, scale bar length is 5 µm. ψ is the angle between the cantilever and the arms of the SRR as depicted in the schematic representation (not to scale). **(b):** Reconstructed image from the scans of rotated SRRs, scale bar length is 5 µm. **(c):** Mean sections between the triangular symbols on (b).

SUPPLEMENTARY MATERIAL FOR IMAGING OF THZ PHOTONIC MODES BY SCATTERING SCANNING NEAR-FIELD OPTICAL MICROSCOPY *

L. Thomas †, T. Hannotte †, C. N. Santos †, M. Lavancier, S. Eliet, M. Faucher, J.-F. Lampin, R. Peretti
Institut d'Electronique, de Microélectronique et de Nanotechnologie,
CNRS, Univ. Lille,
Villeneuve d'Ascq, 59652 France

B. Walter
vMicro SAS
Villeneuve d'Ascq, 59650 France

Corresponding author
romain.peretti@iemn.univ-lille1.fr
† Authors contributed equally to this work

1 Additional information on the FDTD computations

The scan line on a SRR was computed following the procedure described here: Starting from the experimental setup, during the s-SNOM experiment, the vertical motion of the tip can be written as eq. 1, with A the amplitude of the oscillations and Ω the eigenfrequency of the probe. The taylor serie of the exponential dependency of the received scattered NF intensity as the tip approaches the sample can be written as eq. 2., with a, b and c being constants for a given (x, y) position of the tip. Using eq. 1 and 2, the intensity can be rewritten as eq. 3 and the amplitude signal demodulated at the second harmonic of the oscillations of the probe (S_2) as eq. 4.

$$z(t) = A\cos(\Omega t), \tag{1}$$

$$I(t) = az(t)^2 + bz(t) + c, \tag{2}$$

$$I(t) = a\frac{A^2}{2}\cos(2\Omega t) + bA\cos(\Omega t) + ca\frac{A^2}{2}, \tag{3}$$

$$S_2 = \left|a\frac{A^2}{2}\right|. \tag{4}$$

On 20 points along the N-S axis, the intensity received at 45° with respect to the N-S axis was calculated for 4 vertical positions of the tip. From this 4 values, following eq 2, the a, b and c constants where determined by a polynomial regression (2$^{\text{nd}}$ degree) and the first was used to calculate S_2 following eq. 4.

* *Citation*: **L. Thomas, T. Hannotte, C. N. Santos *et al.*. Imaging of THz Photonic Modes by Scattering Scanning Near-field Optical Microscopy. Pages.... DOI:000000/11111.**

Table S1: Dimensions of the images and number of lateral px for averaged sections

Figure	Dimension (px)	(Length) Width of mean section (px)
Figure 2 b, d, left panel Figure S2, a – d, left panel	320 × 256	
Figure 2 b, d, right panel Figure S2, a – d, right panel	256 × 256	
Figure 2 c, bottom panel		3
Figure 3 b, c Figure S3 a, all panels	256 × 256	
Figure 3 d, center panel Figure 3 d, bottom panel Figure S3 b		6
Figure 3 e	200 × 200	
Figure S4, all panels		(256) 6
Figure S5 a Figure S6 a	256 × 256	
Figure S5 b Figure S6 b		6
Figure S7 a Figure S7 b	512 × 512	
Figure S7 c		12
Figure S8 a, all panels	512 × 512	
Figure S8 b		12
Figure S9 a	128 × 128	
Figure S9 b		3
Figure 4 b		(64) 3
Figure 5 a, all panels	256 × 256	
Figure 5 b	195 × 195	
Figure 5 c		6

2 Additional information on the s-SNOM measurements

Additional information on the Lprobes used in this work can be found elsewhere[1]. Images were processed with the Gwyddion software to correct typical artifacts on topographies and analyze data[2]. Except specified otherwise, S_n images are raw data.

The resolution (px) of each image and the width of averaged sections are given in table S1.

3 Computed and THz-TDS transmission of the THz resonators

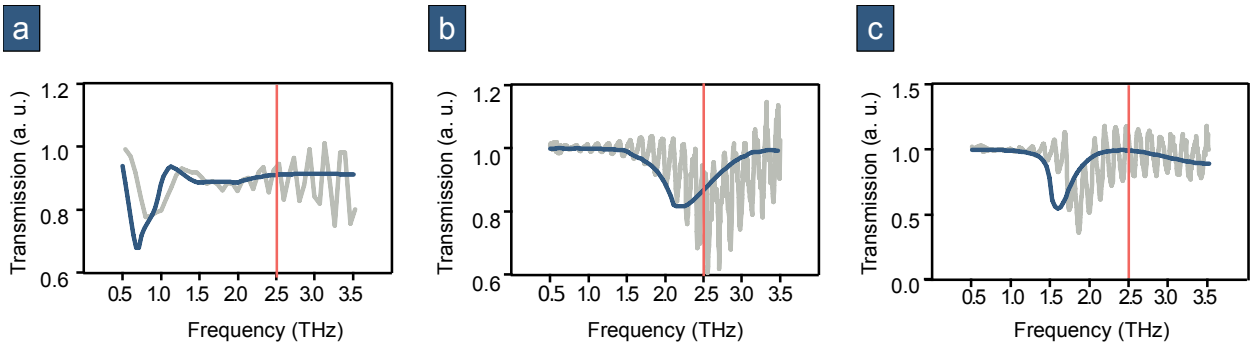

Figure S1: **Accordance of the transmission between simulations and manufactured resonators probed by THz-TDS. (a):** Dark blue line: Computed transmission spectra of an array of LSAs. Grey line: THz-TDS spectra of an array of LSAs. **(b):** The same than (a) for array of SRRs tuned to 2.5 THz. **(c):** The same than (a) for array of detuned SRRs. Red lines mark the emission frequency (2.5 THz) of the THz source used in s-SNOM experiments.

4 s-SNOM images of LSA for all recovered harmonics

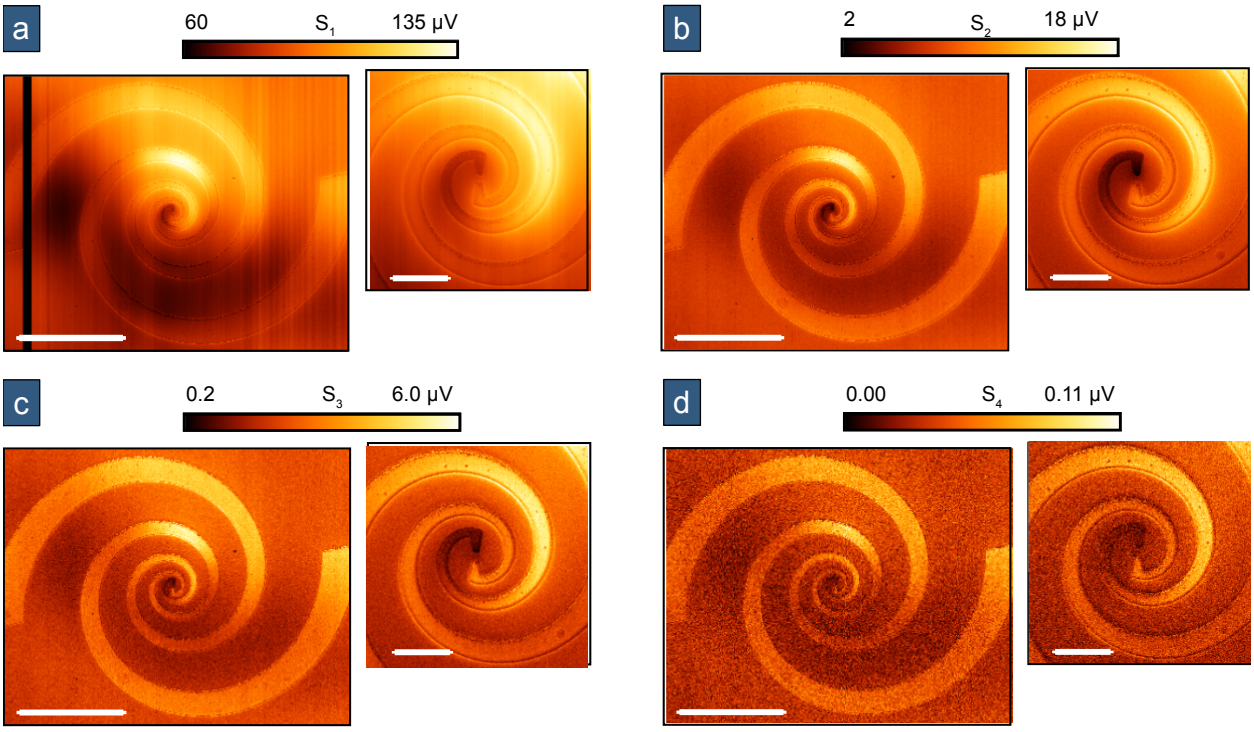

Figure S2: **The same patterns are found on the LSA on all harmonics:** Left panels: large scale s-SNOM images, scale bar length is 30 µm. Right panels: detail of the center, scale bar length is 5 µm: **(a):** 1st harmonic. **(b):** 2nd harmonic. **(c):** 3rd harmonic. **(d):** 4th harmonic.

5 s-SNOM images of a tuned SRR on HR-Si for all recovered harmonics

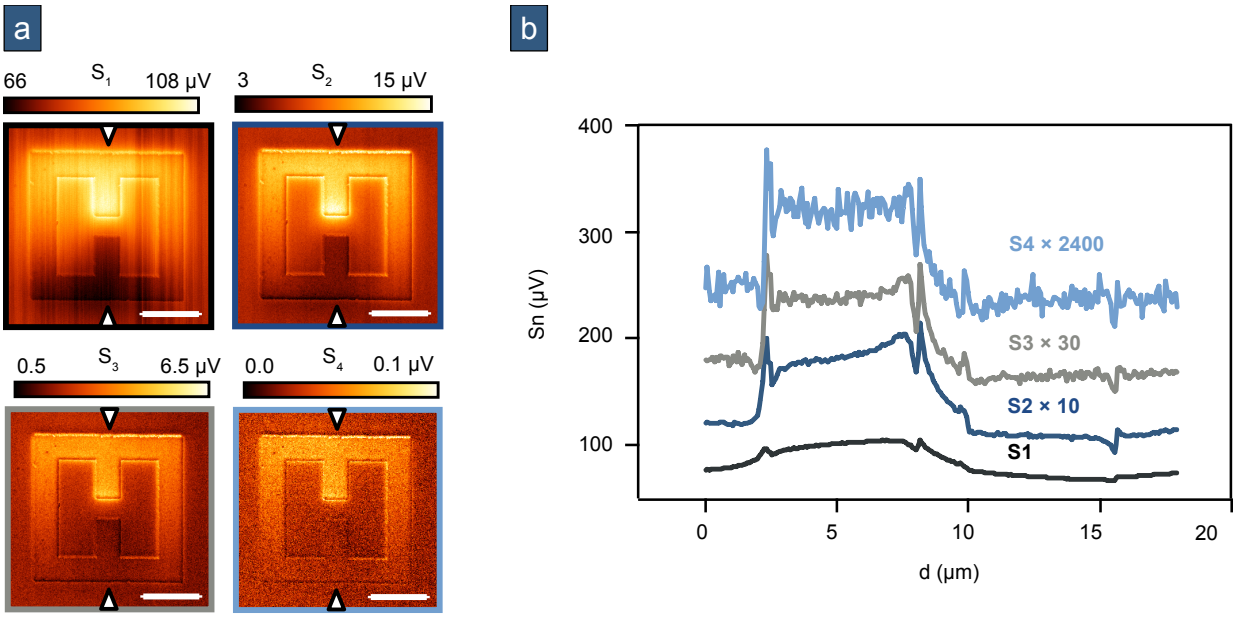

Figure S3: **Asymmetry is found on all recovered harmonics : (a):** s-SNOM images of a tuned SRR (l = 13 µm, g = 2 µm), scale bar length is 5 µm. Optical signal are demodulated at the frequency of the 1st to the 4th harmonic of the cantilever oscillations. **(b):** Mean sections following triangular symbols on (a). Each harmonic has a 60 µV offset.

6 Commented sections along the arms of a tuned SRR on HR-Si

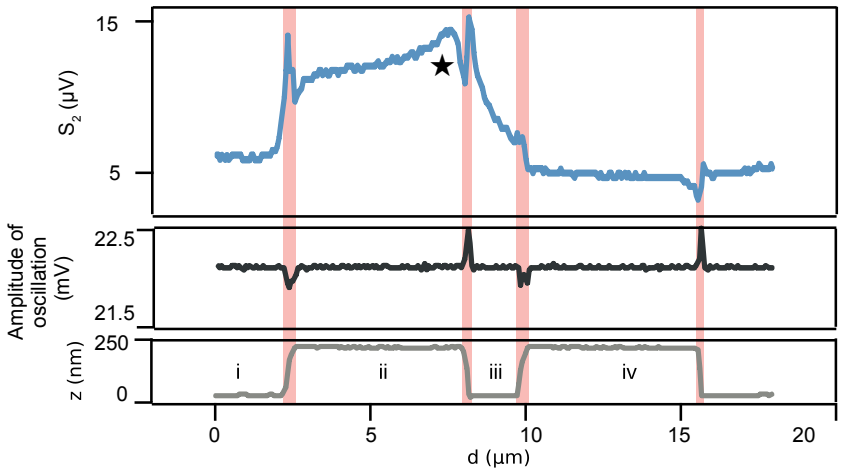

Figure S4: **Identification of the patterns:** Mean sections on the arms of a tuned SRR. Top panel: S_2. Black star indicates the local maximum. Center panel: Amplitude of the oscillations of the probe. Bottom panel: topography. Regions colored in red correspond to the deviation of the oscillations of the probe with respect to the setpoint value when encountering an edge.

On Figure S4, regions labeled i is the surrounding substrate, iii and iv are respectively the N and S arms of the capacitor and region iii is the gap. Between each region the tip encounters an edge of the SRR, resulting a shift of its amplitude of

oscillation and a fringe artifact on S_2. At the location of the local maxima, the tip is far from the edge and amplitude of its oscillations is kept at its setpoint value. Deviating from expectations is the extinction of the right arm (iv) appearing darker than the substrate on S_2.

7 s-SNOM image of a detuned SRR on HR-Si

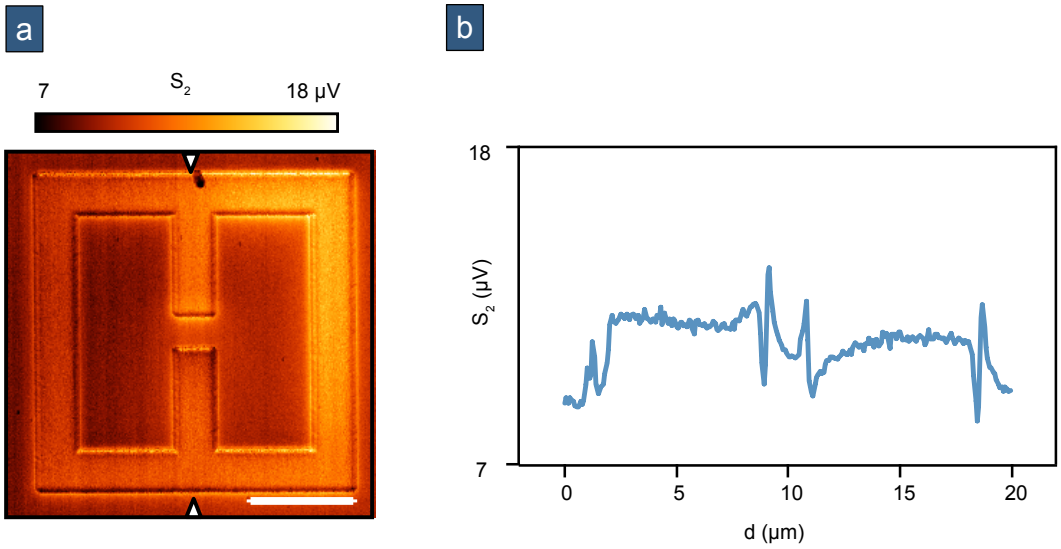

Figure S5: **Detuned SRRs do not show the features observed on the tuned SRRs: (a):** s-SNOM image of a detuned SRR (l = 17 μm, g = 2 μm), scale bar length is 5 μm. **(b):** Mean section (6 px) between triangular symbols on (a).

The scan of the detuned SRR (Figure S5, a) exhibited a slighter contrast with the substrate on the N arm (C: +29 %), compared to the same region for the tuned SRR (C: +111 %). Albeit not extinct, the S arm of the detuned SRR shows less contrast than the N arm (C: +12 %). The contrast in the gap, with respect to the surrounding HR-Si (C: +11 %), is similar to the tuned SRR (C: + 23 %). Section along the arms essentially shows artifacts at the edges of the resonator (Figure S5, b). The main feature of the image is a brighter region on the right of the SRR (C: +37 %). The settings were identical for the two experiments.

8 s-SNOM image of an isolated tuned SRR on HR-Si

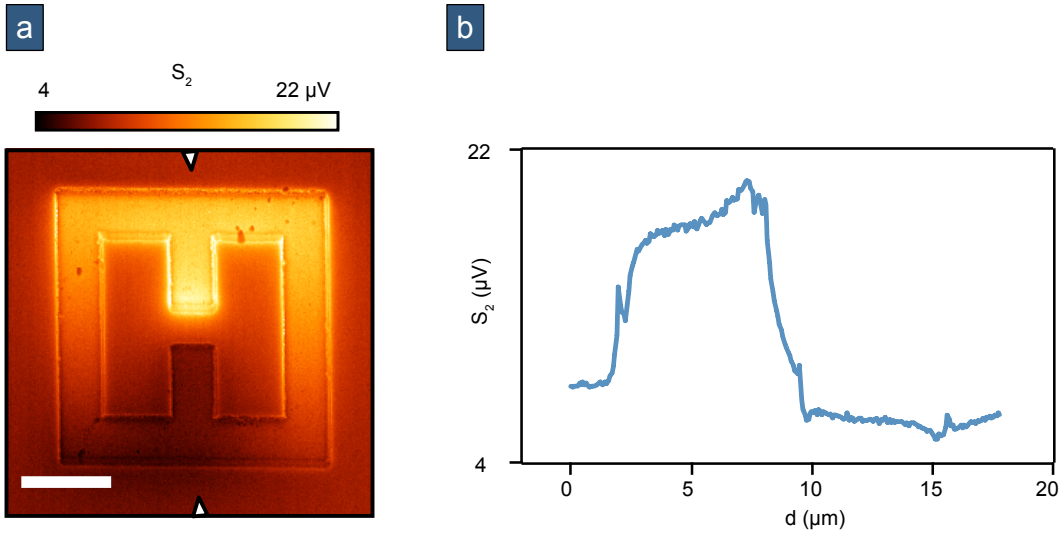

Figure S6: **Isolated SRRs show the same features than SRRs in metasurfaces with the same amplitude : (a):** s-SNOM image of an isolated tuned SRR (l = 13 µm, g = 2 µm), scale bar length is 5 µm. **(b):** Mean section (6 px) between triangular symbols on (a).

We scanned an isolated tuned SRR under the same conditions than the tuned SRR in a metasurface (Figure S6, a, b). The N-S asymmetry (C: +111 % on the N arm, -6 % on the S arm) is the same than observed on the meta-atom. The amplitude of the s-SNOM signal on the isolated SRR is also identical.

9 s-SNOM images of an isolated tuned SRR on HR-Si by HD and PHD

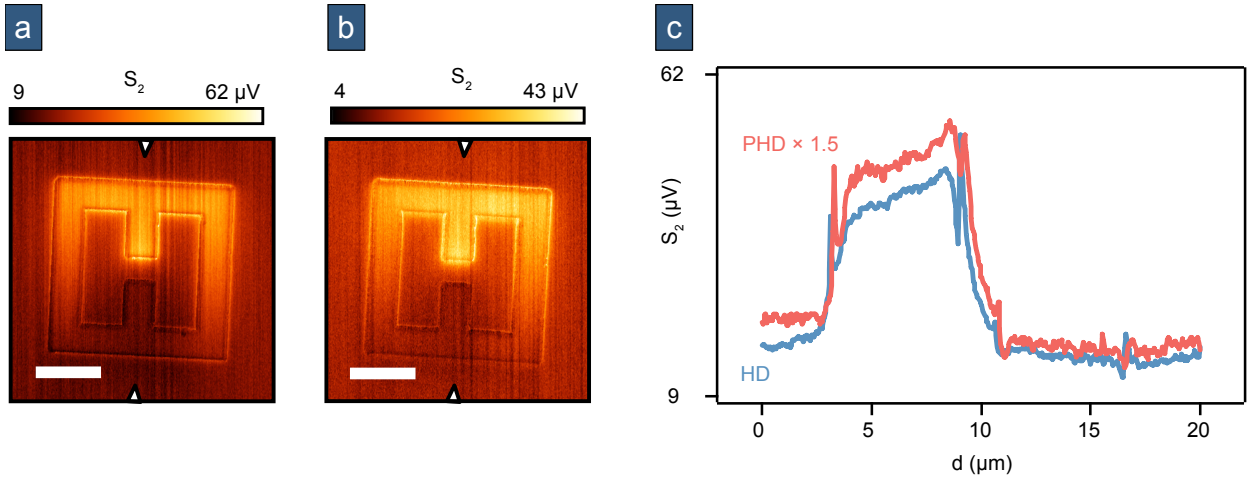

Figure S7: **PHD reveals the same patterns than HD: (a):** s-SNOM image by HD of a tuned SRR (l = 13 µm, g = 2 µm), scale bar length is 5 µm). **(b):** The same device than (a) imaged by PHD. **(c):** Mean sections following triangular symbols on (a) and (b). Blue line: HD, red line: PHD.

S_2 images of an isolated tuned SRR show the same pattern with the same contrast by HD (Figure S7, a, c) and PHD (Figure S7, b, c) (C respectively, for HD and PHD, +119 and +115 % on the N arm and -1 and -6 % on the S arm) Phase could note be recovered by PHD on the S arm due to low signal intensity.

10 s-SNOM images of tuned and detuned SRR on α-SiO_2

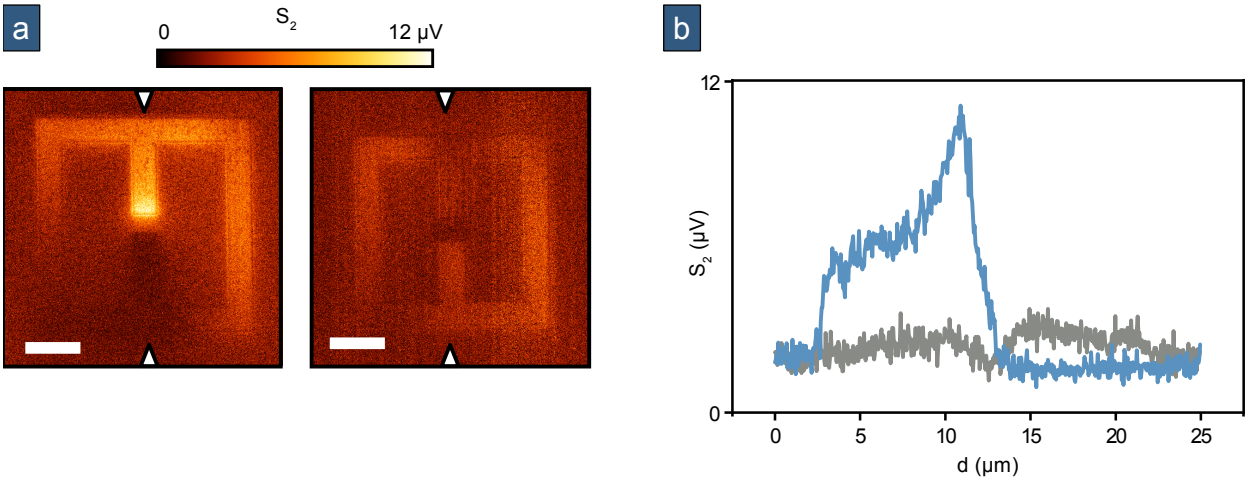

Figure S8: **The same results are obtained on a α-SiO_2 substrate : (a):** s-SNOM image of a tuned SRR on α-SiO_2 (l = 19 µm, g = 2 µm), scale bar length is 5 µm. **(b):** The same than (a) for a detuned SRR (l = 17 µm, g = 2 µm). **(c):** Mean sections following triangular symbols on (a). Blue line: tuned SRR, grey line: detuned.

Following the same route, we designed and fabricated tuned (l = 19 µm, g = 2 µm) and detuned (l = 17 µm, g = 2 µm) SRRs on α-SiO_2. Resonators, assembled in metasurfaces, were fabricated following a procedure reported elsewhere [3]. THz s-SNOM images of tuned and detuned SRRs on α-SiO_2 (Figure S8, a, b) revealed the same features than on HR-Si (C respectively, for tuned and detuned SRR, +244 and +18 % on the N arm and -19 and +33 % on the S arm. For the detuned SRR, the right side is +66% brighter than α-SiO_2).

11 s-SNOM images of a tuned SRR on α-SiO_2 imaged with a shorter probe

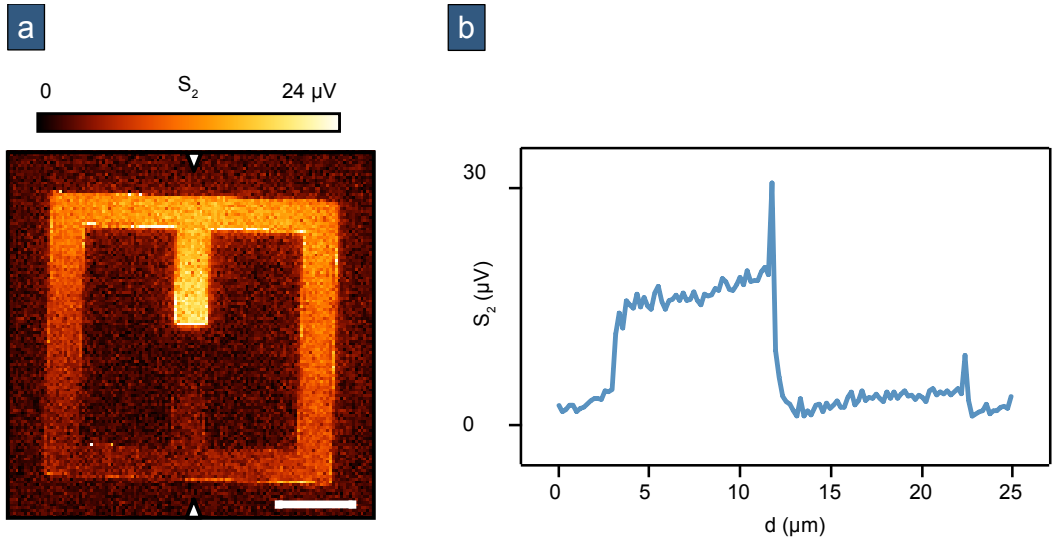

Figure S9: **Asymmetric images are also recorded with shorter probes : (a):** s-SNOM image of a tuned SRR on α-SiO_2 (l = 19 µm, g = 2 µm), scale bar length is 5 µm. **(b):** Mean section following triangular symbols on (a).

On α-SiO_2, a tuned SRR was imaged with a shorter probe (Figure S9, a, b). The probe is an Arrow NCPt from NanoWorld (10 – 15 µm pyramidal tip). Image also exhibited the N-S contrast with higher amplitude (C: +601 %

between the N arm and α-SiO_2, +60 % between the S arm and α-SiO_2). Albeit showing higher contrast, using a shorter probe did not allowed to image the local maximum on the N arm.

Table S2: Recorded contrasts on the s-SNOM images

Region	C**(%)**
Sample: LSA (large scan) – Figure 2	
Max. on arm A	+35
Max. on arm B	+49
Sample: LSA (small scan) – Figure 2	
Probe of arm A	-43
Probe of arm B	+18
Sample: Tuned SRR in metasurface on HR-Si – Figure 3	
Arm N	+111
gap	+23
Arm S	-9
Sample: Detuned SRR in metasurface on HR-Si – Figure S5	
Arm N	+29
gap	+11
Arm S	+12
Right side	+37
Sample: Tuned SRR isolated on HR-Si – Figure S6	
Arm N	+111
Arm S	-6
Sample: Tuned SRR isolated on HR-Si (HD) – Figure S7	
Arm N	+119
Arm S	-1
Sample: Tuned SRR isolated on HR-Si (PHD) – Figure S7	
Arm N	+115
Arm S	-6
Sample: Tuned SRR in metasurface on α-SiO_2 – Figure S8	
Arm N	+244
Arm S	-19
Sample: Detuned SRR in metasurface on α-SiO_2 – Figure S8	
Arm N	+18
Arm S	+33
Right side	+66
Sample: Tuned SRR in metasurface on α-SiO_2 (imaged with shorter probe) – Figure S9	
Arm N	+601
Arm S	+60

References

[1] B. Walter, E. Mairiaux, D. Vignaud, S. Eliet, J.-F. Lampin, and M. Faucher. Terahertz near-field imaging using batch-fabricated cantilevers with 70 µm long tips. In *2019 44th International Conference on Infrared, Millimeter, and Terahertz Waves (IRMMW-THz)*, pages 1–2, September 2019.

[2] Petr Klapetek. *Quantitative data processing in scanning probe microscopy*. Elsevier, 2013.

[3] Théo Hannotte, Louis Thomas, Mélanie Lavancier, Sergey Mitryukovskiy, Jean-Francois Lampin, and Romain Peretti. Towards broadband THz spectroscopy and analysis of subwavelength size biological samples. In Mona Jarrahi, Dmitry Turchinovich, and Sascha Preu, editors, *Terahertz Photonics*, page 2, Online Only, France, March 2020. SPIE.